JOURNAL OF SPACECRAFT AND ROCKETS
Vol. 63, No. 4, July–August 2026

Improving Electron Emission Observability for Spacecraft Touchless Potential Sensing

Kaylee Champion* and Hanspeter Schaub†
University of Colorado Boulder, Boulder, Colorado 80303

https://doi.org/10.2514/1.A36576

Touchless potential sensing allows a servicing spacecraft to determine the electrostatic potential of a nearby target without physical contact. This enables safer docking conditions and electrostatic actuation. While previous studies demonstrate that secondary electron and photoelectron emissions can be used to determine the potential of a target, the emissions may only be observable at 10% of locations about a target. This paper researches sensing strategies for the servicer position and beam parameters to enhance the detection of electron emissions in the presence of complex geometries and differential potentials. Using validated SIMION simulations, it is shown that increasing the half angle of an electron beam or vacuum ultraviolet laser from 0.2 to 2 deg and sweeping through deflection angles can nearly double the number of detectable positions. Additionally, the study examines how differential surface potentials shift or suppress electron emission trajectories, changing the observability. It is found that using an ultraviolet laser to excite emissions from a differentially charged target can excite detectable emissions for more than double the conditions in which an electron beam can excite detectable emissions. The results provide guidance for improving the effectiveness of touchless potential sensing in Geosynchronous Earth Orbit and cislunar operations, especially for servicing and docking missions.

Nomenclature

A	=	emission area, m^2
B	=	magnetic field strength, T
D	=	spacing, m
E	=	energy of particles, eV
f	=	particle flux, s/s
I	=	particle current, A
m	=	mass of a charged particle, kg
N	=	number of particles in a sphere
n	=	charged particle number density, m^{-3}
R_{eff}	=	effective sphere radius, m
r_g	=	gyroradius, m
T	=	charged particle temperature, eV
V	=	surface potential, V
v	=	velocity of a charged particle, $m \cdot s^{-1}$
α	=	total electron emission yield due to ambient electrons
γ	=	deflection angle of equipment, deg
δ	=	secondary electron yield
η	=	backscattered electron yield
λ	=	length, m
ϕ	=	half angle of equipment, deg

Subscripts

B	=	beam
D	=	Debye
e	=	electrons
G	=	gap
i	=	ions
ph	=	photoelectrons
S	=	servicer
se	=	secondary electrons
T	=	target

I. Introduction

INTERACTIONS between spacecraft, energetic plasma, and the radiation environment generate surface currents and potentials. The magnitude of the surface potential on a spacecraft is highly dependent on its geometry, material properties, and sunlit area [1,2]. High-altitude Earth orbits, geosynchronous Earth orbit (GEO), and some cislunar regions, such as the plasma sheet, are considered hazardous charging environments, with possible charging levels on the order of tens of kilovolts [3,4]. Two spacecraft or electrically disconnected surfaces in the same environment may charge differently [5,6], and a significant potential difference between nearby surfaces or contact between differently charged surfaces can cause arc discharges, potentially damaging electronics and ending missions [7–9]. This is particularly dangerous during docking operations, as a damaging arc discharge may occur between two spacecraft with different potentials upon contact. In addition, charged spacecraft exert electrostatic forces and torques on each other during proximity operations. This causes unexpected deflections, requiring more fuel to maintain the desired positions [10,11]. Conversely, the electrostatic force between two spacecraft can be used for touchless applications such as moving space debris [12–16] and detumbling a target [17–20]. This process is referred to as electrostatic actuation.

Knowledge of a neighboring spacecraft's potential can be used to avoid arc discharges when docking or to enable electrostatic actuation. Spacecraft–plasma interaction codes such as Nascap-2k [21] and Spacecraft–Plasma Interaction Software (SPIS) [22] have been developed and widely used to model spacecraft charging. These codes are useful resources to generate a reasonable range of expected surface potentials and develop a deeper understanding of the spacecraft charging process. However, surface material and plasma properties vary significantly in space through processes such as material degradation and solar storms [23–25], and these charging codes use simplifying assumptions to increase the efficiency of computations, introducing uncertainty. Therefore, an in situ method of detecting neighboring spacecraft potentials is necessary for an accurate assessment of arc discharging hazards and electrostatic forces during proximity operations.

Several techniques have been proposed to determine the potential of a spacecraft or surface without making contact with the surface.

Presented as Paper 2023-1770 at the AIAA SciTech 2023 Forum and Exposition, National Harbor, MD, January 23–28, 2023; received 6 August 2025; accepted for publication 10 January 2026; published online 26 March 2026.

*NASA Space Technology Graduate Research Opportunity Fellow, Graduate Research Assistant, Department of Aerospace Engineering Sciences; kaylee.champion@colorado.edu. Student Member AIAA.

†Distinguished Professor and Department Chair, Schaden Leadership Chair, Department of Aerospace Engineering Sciences. Fellow AIAA.

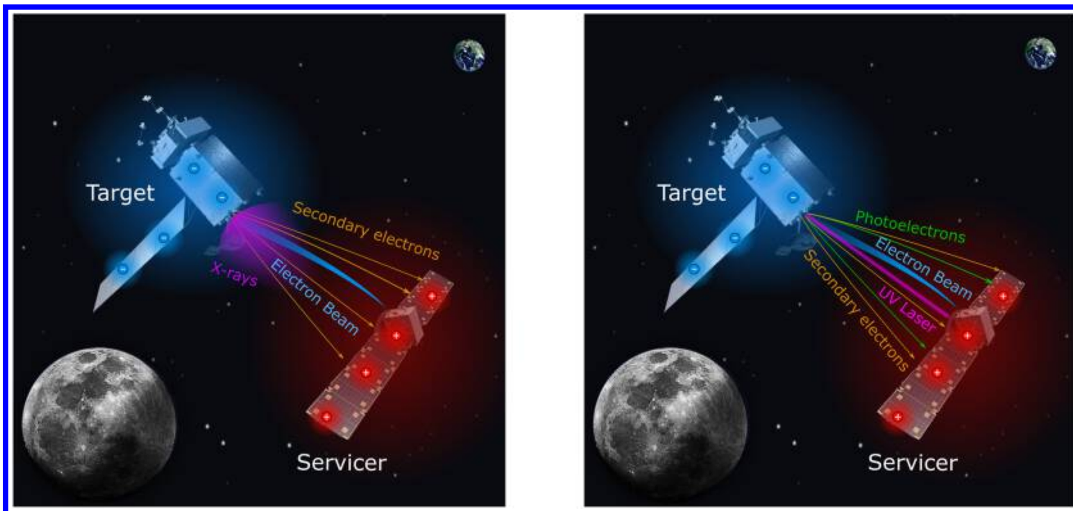

a) Secondary electron and x-ray method **b) Secondary electron and photoelectron method**

Fig. 1 Active potential sensing concepts using an electron beam and VUV laser.

Ferguson et al. propose using ground-surface material glow, bremsstrahlung x-ray emissions, and radio and optical emissions from arcs to estimate the surface charging and arcing behavior of spacecraft in GEO from the ground or low Earth orbit [26]. Lunar Probe Electron Reflectometer data are utilized to study the energy-dependent electron loss cone and secondary electrons accelerated from the lunar surface to determine the difference in potential between the lunar surface and the spacecraft [27–31]. In experiments, technologies such as noncontact voltmeters, scanning electron microscopes, and electrostatic probes are utilized to contactlessly determine surface potential at separation distances of millimeters to centimeters [32–35].

Touchless potential sensing techniques have been investigated to determine the potential of a neighboring spacecraft in geosynchronous and cislunar regions at separation distances of tens of meters. These techniques involve a servicing spacecraft aiming an electron beam at a target spacecraft to excite secondary electron (SE) [36–39] and x-ray emissions [40–43] (Fig. 1). Alternatively, a vacuum ultraviolet (VUV) laser can be used to excite photoelectron (PE) emissions [44]. The energies of the emissions are measured by the servicer using an electrostatic-analyzer-type instrument, such as a retarding potential analyzer (RPA), and are used to determine the potential of the target with respect to the servicer. Existing tools such as RPAs [45], electron spectrometers [46], and electric field double probes [47] allow the servicer to determine its own potential. Once the potential of the servicer and the difference in potential between the two crafts are known, the potential of the target can be deduced.

The methods for touchless potential sensing (SE, PE, and x-ray) have varying benefits and challenges. SEs and PEs allow for the most accurate estimation of the target's potential (within tens of volts), while x-ray emissions have errors on the order of 100 volts [48]. X-ray emissions favor higher-energy electron beams and can be detected as long as the electron beam impacts the target [43,48]. Electron emission trajectories are highly dependent on the target geometry and can only be detected at a fraction of positions around the object. In addition, SE emissions favor low-energy electron beams that are more susceptible to deflection by the electric field about the spacecraft. Around a uniformly charged target, secondaries have been detected at ≈10% of relative locations in experiments [38,39]. VUV lasers are not deflected by the ambient electric field, so PE emissions have been detected at ≈20% of relative locations in experiments with a uniformly charged target [44]. NASA guidelines indicate that all surface materials should be conductive and electrically connected to generate a uniform potential across the spacecraft [3], but degraded electrical bondings, surface dielectrics, and high-voltage solar panels may cause different potentials to form on varying spacecraft surfaces. Detecting electron emissions becomes even more difficult once differential potentials arise, as the changing electric field suppresses electron emissions and alters the emission trajectories [39,49].

The *observability* of a target spacecraft is defined in this project as the fraction of relative positions in which emissions can be detected for touchless potential sensing. As previously mentioned, electron emissions typically have low observability, making it the limiting factor for touchless potential sensing. Previous work has characterized electron trajectories about objects of varying shapes [49], compared and combined sensing using SE and x-ray emissions [48], and revealed that differential potentials on a spacecraft can prevent electron emissions from leaving a target's surface [39]. However, strategies to actively increase the observability of a target's electron emissions have not been investigated.

This paper introduces an investigation into sensing strategies that actively improve the observability of electron emissions by positioning the servicing spacecraft and manipulating the electron beam and VUV laser parameters. Specifically, it is examined how the servicer's position and equipment parameters change the detected electron emission current, especially in the presence of differentially charged components. This is the first comprehensive analysis of how equipment and operational configurations can be tailored to enhance the effectiveness of touchless potential sensing in realistic, high-potential orbital environments.

Particle-tracing simulations in SIMION have recently been validated for the study of the charged-particle dynamics problem using vacuum chamber experiments [39,44]. These simulations are extended to a "full-scale" model of meters-long spacecraft separated by tens of meters during touchless potential sensing operations in Sec. II. The impact of the spacecraft potentials on the observability of the target spacecraft is investigated in Sec. III. Section IV presents the manner in which electron beam and VUV laser parameters should be manipulated to excite detectable emissions. The servicer and target charging behavior during touchless potential sensing using an electron beam is investigated in Sec. V.

II. Modeling Approach

The numerical model of touchless electrostatic potential sensing is developed in SIMION[‡] software, a charged-particle trajectory software package, by means of Lua user-defined functions. Previous work presents detailed descriptions of the emission process and related SIMION particle-tracing simulations for SEs [39] and PEs [44], which are implemented in this paper.

[‡]https://simion.com/.

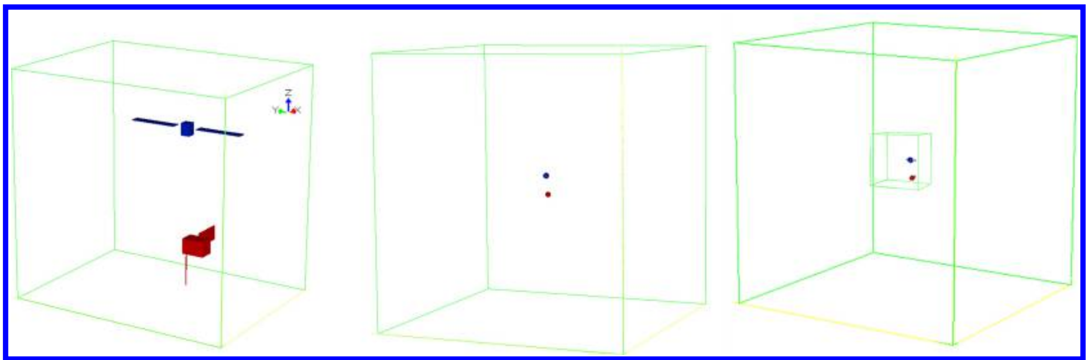

Fig. 2 **SIMION spacecraft fine and coarse PAs and an initialization of the fine PA in the coarse PA.**

A. Electrostatic Framework

SIMION computes the trajectory of each charged particle from Newton's second law:

$$\frac{d\boldsymbol{v}}{dt} = \frac{q}{m}\boldsymbol{E} \tag{1}$$

where $\boldsymbol{v}$, q, and m are the particle velocity, charge, and mass, respectively; $\boldsymbol{E}$ is the electric field; and t is the time. Relativistic corrections are implemented when v^2/c^2 exceeds 10^{-10}, with c being the speed of light. The electric field is derived from the electrostatic potential field V as

$$\boldsymbol{E} = \nabla V \tag{2}$$

while V is computed by solving Laplace's equation,

$$\nabla^2 V = 0 \tag{3}$$

in the simulation domain. SIMION employs a Cartesian mesh, and the electric-field boundary conditions are determined by a constant potential (Dirichlet) or a constant electric field (Neumann). The potentials of components can be individually adjusted in SIMION, and the additive property of the Laplace equation is utilized to determine the potential field, which is saved as a *potential array* (PA).

B. Potential Field Generation

To appropriately model the potential field around a spacecraft in a plasma environment, the boundary must be defined sufficiently far away such that the boundary conditions do not significantly impact the potential field calculations. In space environments, the appropriate distance is often defined by the Debye length λ_D, an approximation of how far a charge's electrostatic effect persists [50]. In other words, a Dirichlet boundary condition of 0 V is defined approximately λ_D from the spacecraft. In hazardous charging environments, such as GEO and the cislunar plasma sheet and magnetotail lobe regions, the Debye length ranges from ≈100 m to several hundred meters based on parameters from [3,25,51]. To properly define the spacecraft components, elements on the order of centimeters are required, but defining a computational space with a width of several hundred meters using centimeter-sized elements is computationally inefficient. Therefore, a *fine PA* with a resolution of centimeters is defined within a *coarse PA* with a resolution of meters, as shown in Fig. 2. The internal fine PA captures the nearby potential field due to the geometry of the system, while the outer, coarse PA captures the decay of the electrostatic potential field.[§]

In the fine PA, spacecraft are defined according to their geometry (Fig. 2a). To generate the entire electrostatic field with elements on the order of a few meters, the spacecraft are defined in the coarse PA as spheres with equivalent self-capacitance as the spacecraft models (Fig. 2b), referred to as effective spheres. The self-capacitance of the spacecraft is found using the multisphere method (MSM) [52–54], and the radius R_{eff} of a single sphere with equivalent capacitance C to the complex-geometry spacecraft in the fine PA is

$$R_{\text{eff}} = \frac{C}{4\pi\epsilon_0} \tag{4}$$

where ϵ_0 is the permittivity of free space.

The size of the fine PA is variable to optimize computational efficiency without sacrificing accuracy. The boundary is defined to be approximately three spacecraft widths from the complex-geometry models because the electrostatic environment surrounding complex spacecraft shapes can be approximated with an effective sphere if the distance is larger than 2–3 craft radii [55,56]. The width of the spacecraft is defined using the longest end-to-end distance of the spacecraft (typically tens of meters) to ensure that changes in attitude do not decrease the distance from the spacecraft surface to the fine PA boundary.

The target's position and attitude in the fine PA are held constant to keep the target's surfaces aligned with the Cartesian PA elements. In SIMION, misalignment with the PA elements results in jagged surfaces that may alter the SE and PE trajectories. To further improve accuracy, the electrode surface enhancement feature is utilized, which allows electrode points to be defined in partial grid units and can improve the accuracy of the potential field by at least an order of magnitude.[¶]

The simulation is initialized with the fine PA positioned such that the spacecraft and their effective spheres in the coarse PA are in the same positions, as shown in Fig. 2c. The potential field surrounding the spherical, charged spacecraft is first solved throughout the entire coarse PA to characterize the general potential field decay. The potential field values from the coarse PA at the location of the fine PA boundary elements are then assigned as Dirichlet boundary conditions on the individual fine PA boundary elements, and the potential field due to the spacecraft geometry in the fine PA is solved. In addition, the effective spheres are set to 0 V and moved such that they are in contact with a corner of the coarse PA to prevent the spheres from influencing the final particle trajectories. Now, the charged particles can be initialized and their trajectories simulated. MATLAB is employed to configure the PA geometry, launch the SIMION simulation, and analyze the results through the use of Windows batch files. This implementation allows several SIMION setups to be defined and automatically run with minimal interference.

C. Mesh Independence Analysis

Analysis is conducted to ensure that the results are consistent independently of the resolution of the mesh. In other words, the

[§]See the SIMION `field_emission` example available with the software for further discussion of a fine PA nested within a coarse PA.

[¶]See the SIMION `surface_enhancement` example available with the software.

mesh size does not change the results of the simulation. In this analysis, the servicer is based on the SSL-1300 spacecraft, and the target is based on the GOES-R spacecraft. The SSL-1300 model consists of a 2.5 m × 2.5 m × 3 m cube main body and two 12.1 m × 2.3 m × 0.4 m solar panels. The GOES-R model consists of a 4 m × 4 m × 6 m main body, an 8.3 m × 4 m × 0.4 m solar panel, and an 8.3 m × 0.4 m × 0.4 m boom. These spacecraft are not intended to exactly match the SSL-1300 and GOES-R spacecraft, only to serve as a general representation of spacecraft that may be found in GEO and cislunar space. The radii of the spheres with equivalent capacitance to the models are 4.80 m for SSL-1300 and 4.44 m for GOES-R.

The servicer can be equipped with an electron gun or VUV laser and is assumed to have aluminum surfaces. For this setup, the Sanders and Inouye SE yield model is used to define the secondary electron yield as a function of beam energy. The maximum yield $\delta_{\max}$ and the energy at maximum yield $E_{\max}$ are set at 0.97 and 300 eV, respectively, based on the values for aluminum [1]. A photoelectron emission effective yield of 0.058 and reflectance of 0.85 for the VUV laser defined in Sec. IV are implemented [44,57].

It is desirable to make the computations as efficient as possible without sacrificing accuracy; therefore, the element size is halved, or the resolution is doubled, until the solution is altered by less than 10% by increasing the resolution. This is done for a separation distance of 20 m between a −4 kV servicer and a −13 kV target with the servicer's electron beam pointing directly at the target's body. An electron beam energy of 11 keV is utilized, and the number of secondaries impacting the 2.5 × 2.5 m side of the servicer's body facing the target is recorded. Table 1 shows the results of the mesh independence analysis with the final element and boundary sizes.

Table 1 Mesh independence analysis

Parameter	Initial size	Initial run time, s	Final size	Final run time, s	Detected SE percent difference, %
Final PA element size	20 cm	20	40 cm	10	5
Coarse PA element size	1 m	40	2 m	10	8
Boundary distance	400 m	40	200 m	10	3

D. Differentially Charged Spacecraft

Modeling spacecraft with differential potentials introduces another level of complexity to the SIMION simulations because the singular sphere used to determine the coarse PA cannot be used to represent multiple potentials. To resolve this, representative spheres of each component of the spacecraft are generated and utilized for the coarse PA. The GOES-R model represents the target in this project, so the solar panel and boom can charge independently of all other components. The representative spheres have radii of 2.96, 2.49, and 1.21 m for the main body, solar panel, and boom, respectively. The spheres are then placed at the center point of the component's location, and the coarse PA and fine PA are resolved as previously described. To ensure that this is appropriate, a potential of −13 kV is set for all components of the target and −4 kV for the servicer, and the simulation described in the previous section is repeated. It is found that the detected secondaries remain the same, validating that discretizing the spheres in the coarse PA is appropriate for modeling differential potentials.

E. Environmental Considerations

The spacecraft–plasma interactions are not included in SIMION; however, the interactions with the ambient space environment in GEO and the cislunar plasma sheet show that this model is appropriate. As previously mentioned, the external boundaries are located approximately a Debye length (≈200 m) from the spacecraft. The separation distances investigated in this project are less than 20 m, approximately an order of magnitude less than the Debye length. Therefore, Debye shielding is considered a secondary effect and can be neglected.

The gyroradius, or the radius of the circular motion of a nonrelativistic charged particle in a magnetic field, is

$$r_g = \frac{v_\perp m_e}{q_e B} \tag{5}$$

where $v_\perp$ is the velocity perpendicular to the magnetic field, m_e is the mass of an electron in kilograms, q_e is the elementary charge, and B is the magnetic field strength in teslas. The thermal velocity of an electron is

$$v_\perp = v_e = \sqrt{\frac{2k_B T_e}{m_e}} \tag{6}$$

where k_B is Boltzmann's constant and T_e is the electron temperature. The geomagnetic field in GEO orbit is 100 nT, resulting in gyroradii of 100–3000 m for electron energies from 10 to 10^4 eV assuming that the electron velocity is entirely perpendicular to the magnetic field [39]. The field in the plasma sheet may be on the order of 20 nT [58], resulting in gyroradii of 355–11,000 m for electron energies from 10 to 10^4 eV. This is again larger than the maximum separation distance and is considered a secondary effect.

The distance at which particles travel between collisions is characterized by the mean free path λ_{mfp}. The mean free path of particles in a Maxwellian plasma is [59]

$$\lambda_{\text{mfp}} = \frac{48\sqrt{6/\pi} N_D \lambda_D}{\ln(9N_D)} \tag{7}$$

where N_D is the Debye number, or the number of particles in a sphere with radius equal to the Debye length

$$N_D = \frac{4}{3}\pi n_e \lambda_D^3 \tag{8}$$

where n_e is the electron number density. The mean free path in GEO is approximately 3.5E5 km for worst-case GEO data and is approximately 2.7E9 km for mean plasma sheet characteristics [51]. Therefore, assuming a collisionless, vacuum model is appropriate in these environments.

The maximum current density that can be emitted across a distance, or the space-charge-limited (SCL) current I_{SCL}, can be estimated with the one-dimensional Child–Langmuir law [60,61]

$$I_{\text{SCL}} = A\frac{4\epsilon_0}{9q_e}\sqrt{\frac{2}{m_e}}\frac{E_B^{3/2}}{D^2}\left(1+\sqrt{1+\frac{q_e V_G}{E_B}}\right)^3 \tag{9}$$

where A is the emission area, E_B is the initial beam energy, D is the gap spacing, and V_G is the gap voltage. In this scenario, the gap spacing is assumed to be the separation distance between the two spacecraft, and the gap voltage is the difference in potentials between the servicing and target spacecraft. The SCL current for a separation distance of 15 m, circular emission areas with a 2 cm radius, and varying beam energies and spacecraft potential differences is shown in Fig. 3. The white region of the plot indicates when the difference in potentials is larger than the beam energy, in which case the beam will not reach the target and will be deflected back toward the servicer [62]. In particular, the space-charge limitation can impede touchless potential sensing if a low-energy, high-current electron beam is utilized. The beam currents utilized for the majority of this work are below the SCL current. It should be noted that beam–plasma instabilities, such as two-stream and electron modulation instabilities, are not considered in this analysis [63–65].

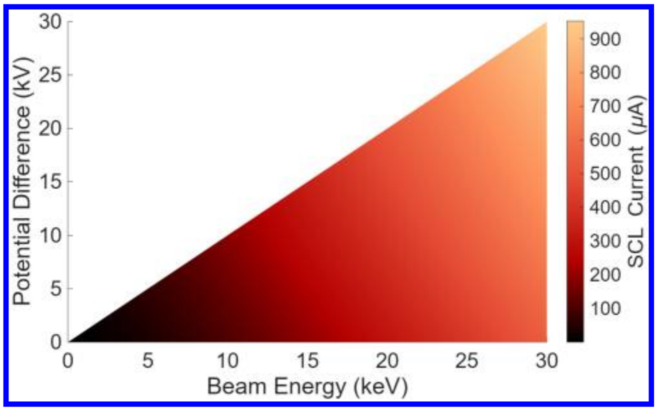

Fig. 3 Space charge limited current for a 2 cm emitter at a separation distance of 15 m.

III. Servicer Relative Position

A. Simulation Setup

The trajectories of electron emissions are highly dependent on the target's geometry. In general, there are regions about a target in which electron emissions can penetrate, while there may be other regions from which the emissions are deflected. This alters the fraction of positions around the target in which the servicer can intercept electron emission trajectories, referred to as the *observability* in this work. The emission trajectories around various spacecraft geometries have previously been investigated [36], and it has been shown that the emission trajectories are independent of the target's potential if the target is uniformly charged [48]. However, these simulations did not include a servicing spacecraft or a differentially charged target. Therefore, the impact of varying servicer and target potentials or differential potentials on the observability without the inclusion of an electron gun or VUV laser is first characterized.

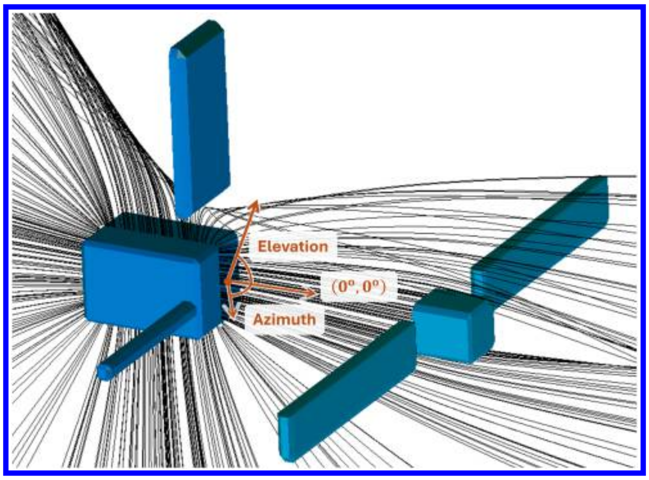

Fig. 4 Vertical cut view of electron emission trajectories (black) between the target (left) and servicer (right).

In this section, low-energy electron emissions are generated uniformly over the main body of a target spacecraft. SE emission energies can be modeled using the Chung–Everhart probability density function, with a peak at one third of the work function of the material [66], and PE emission energies are typically between 1 and 3 eV [67]. Aluminum is assigned as the surface material of the target with a work function of 4 eV [68], so the energy of the electron emissions is defined as 1.333 eV. An example of a vertical cut view of the electron emissions is shown in Fig. 4.

The servicer and target are modeled at a constant center-to-center separation distance of 15 m. In each assigned servicer-and-target surface potential, the servicer is moved through all possible azimuth and elevation angles, ±180 and ±90 deg, respectively, in 10 deg steps while facing the center of the target, for a total of 703 runs in SIMION for each setup. This is equivalent to the target rotating through all positions near a stationary servicer. The target's solar panel is aligned with the 90 deg elevation axis, and the boom is aligned with the −90 deg azimuth axis, as shown in Fig. 4. The number of electrons impacting the surface of the main body of the servicer facing the target is recorded, and the servicer is considered to have detected electron emissions when at least one particle impact is recorded.

B. Uniform Servicer and Target Potentials

To explore the effect of a charged servicer, the potentials of the servicer and target are tested at 1, 2.5, 5, 7.5, and 10 kV and −1, −2.5, −5, −7.5, and −10 kV, respectively, at all relative positions, for a total of 9063 runs.

The observability, shown in Fig. 5a, is generally higher for a more positive servicer and lower for a more negative target, with the highest observability for a −1 kV target and 10 kV servicer and the lowest observability for a −10 kV target and 1 kV servicer. This occurs because the electron emissions are accelerated by the negatively charged target, making them less susceptible to the electric field generated by the servicer's more positive surface potential. Despite this, the fraction of observable locations only varies between 0.67 and 0.75, a 12% change between the worst and best case, which indicates that the spacecraft potentials do not significantly change the emission trajectories. This presents both pros and cons for touchless potential sensing. Unfortunately, biasing a servicer more positively does not significantly increase the observability of a target. However, the regions in which electron emissions should be expected from a uniformly charged target can be determined for one set of servicer and target potentials and reliably utilized to set keep-in and keep-out zones for a servicer during touchless potential

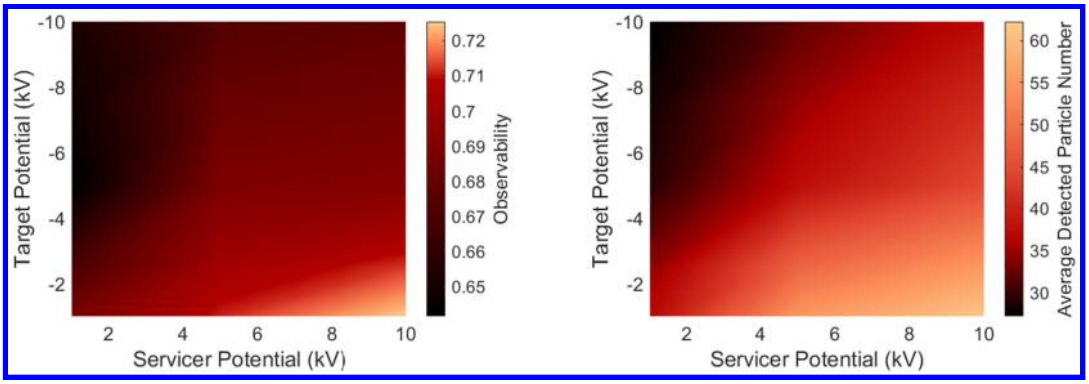

a) Fraction of locations in which electron emissions are observable

b) Average detected particle count

Fig. 5 The fraction of locations particles are detected (left) and average number of particles detected (right).

sensing operations. The regions in which electron emissions can be detected vary for different spacecraft geometries, so this must be determined for specific spacecraft missions.

It can be noted that the observability for this scenario is higher than the 10–20% cited in the introduction. This can be attributed to multiple factors. First, the reported observability in the introduction is recorded for a small box-and-panel representative spacecraft in a vacuum chamber, and the different geometry may generate different emission trajectories. The experimental observations are also conducted on about one two-dimensional plane. In other words, the elevation is zero in the reported experiments, and this path may happen to be one in which electron emissions are significantly repelled from the electron sensor. Finally, the experiments are conducted using an electron beam or VUV laser to emit secondary electron or photoelectron emissions, respectively, which increases the complexity of the problem. The inclusion of a beam to excite emissions is explored in Sec. IV.

Figure 5b shows the average number of particles detected when the target is observable. This is determined by summing the number of particles detected for all servicer positions in a servicer-and-target surface potential configuration and dividing by the number of instances in which the servicer detects a current. The average number of detected particles increases nearly linearly with servicer and target potential. This, combined with the observability results, indicates that the general zones in which the servicer can detect electron emissions remain stable, but a more positive servicer can draw in nearby electron emissions to increase the strength of the signal. This conclusion only holds when the emission current remains the same, as would be expected when actively emitting electrons or detecting naturally emitted PEs. When sensing passively emitted SEs, previous work has shown that increasing the servicer's potential can significantly *decrease* the SE emissions from a target [69].

C. Differential Target Potentials

It is shown that biasing the servicer more positively does not significantly change a target's observability. However, a differentially charged target is expected to alter the electron trajectories and thus the observability. To explore this, the potentials of the target's solar panel and boom are individually varied from −33 to 7 kV (±20 kV with respect to the main body) in 10 kV steps, for a total of 25 surface potential combinations. The target's main body is held at −13 kV, and the servicer is held at −4 kV for all simulations. These values are selected based on the surface potentials expected when the Lunar Gateway and Orion dock [70]. This range of positions and differential potentials results in a total of 17,575 simulations in SIMION.

Nascap-2k simulations completed in Ref. [71] predict maximum differential charging up to 20 kV in GEO substorm conditions. It is likely that, if differential potentials of this magnitude occur, arc discharges or dielectric breakdown would occur and work to resolve the potential difference. Therefore, 20 kV differential potentials serve as a bounding case for what may be expected in GEO-like plasma environments.

Figure 6 shows vertical cut views of electron emissions from the main body of the target with varying component potentials. The electron emissions from the uniformly charged target (Fig. 6a) are deflected by the solar panel and boom. The negatively biased solar panel (Fig. 6b) exacerbates this effect by suppressing electron emissions such that they are reflected back into the surface of the target. This effectively decreases the total emitted current from the main body and further limits the regions in which electron emissions can reach a servicer. Alternatively, if the components are biased more positively than the main body (Fig. 6c), the electrons are attracted toward the components. This widens the regions through which emissions pass, increasing observability. It should be emphasized that the target's components only need to be biased positively with respect to the main body, not with respect to zero, in order for the emissions to be attracted toward the components.

The detected particles for three of the 25 simulated target surface potentials are shown in Fig. 7. For the uniformly charged target (−13 kV components), it is best to be parallel to the flat surfaces of the main body and to maximize the distance from extruding components to the servicer. When both components are negatively biased (−33 kV components), the electrons are repelled at such a magnitude that it is no longer beneficial for the servicer to be

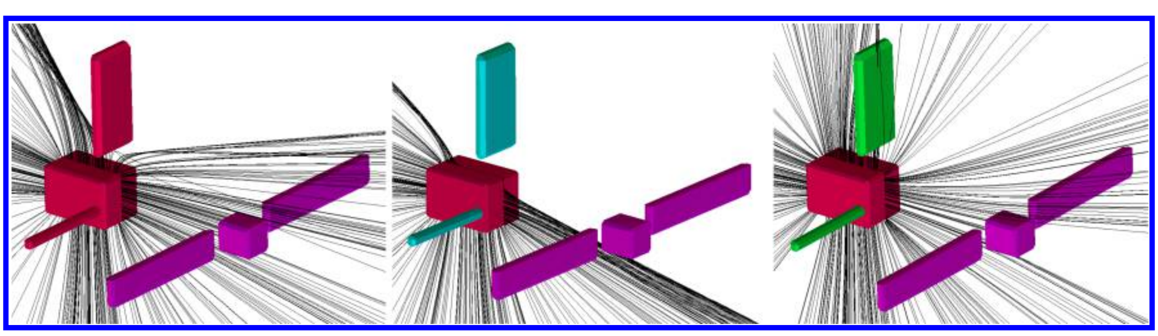

a) -13 kV components b) -23 kV components c) -3 kV components

Fig. 6 Vertical plane of electron trajectories (black) between a target (left) with variable component potentials and a servicer (right).

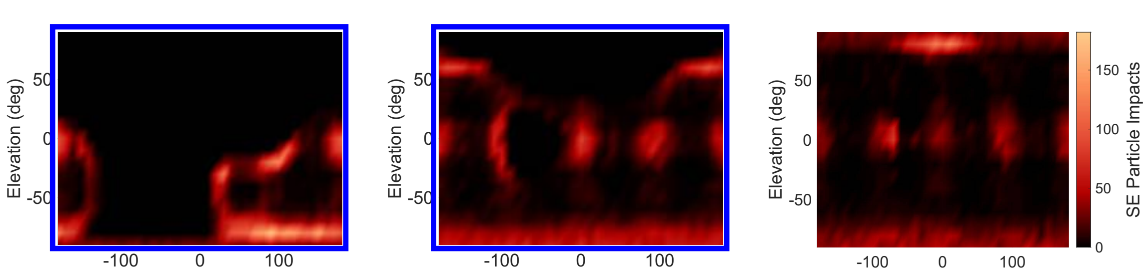

a) -33 kV components b) -13 kV components c) 7 kV components

Fig. 7 Number of electron emission particles from a target with a main body of −13 kV detected by a −4 kV servicer.

parallel to a flat surface of the target. In this case, the servicer should instead prioritize maximizing the distance from the components to the servicer. Furthermore, the concentration of electron emissions is largest for the most negative components, despite the fact that some of the electron emissions are deflected back into the surface of the target. In other words, the negative components act as a focusing mechanism, which can increase the detected electron emission current. Conversely, when both components are positively biased (7 kV components), it again becomes beneficial for the servicer to position itself parallel to the flat surface. However, the optimal positions are near the components, not farther away, and the magnitude of particle impacts is lower in nearly all detectable regions.

These results indicate that, if a target is differentially charged, the regions in which electron emissions can be detected are no longer consistent. Fortunately, there may be regions in which electron emissions are more likely to be detected despite differential potentials. Figure 8 shows the number of target surface potential combinations, referred to as instances in the color bar, in which electron emissions can reach the servicer at each location. There are a total of 25 differential potential setups tested for the target. So, if 25 detectable instances occur at a specified azimuth and elevation, then emissions can be detected for all target differential potentials tested. There are 25 detectable instances in the locations circling ≈130 deg azimuth and −40 deg elevation. In this area, the servicer is near the corner of the target's main body opposite the servicer and boom. This effectively shields the electron emissions from the target component's electric field, allowing the servicer to detect emissions regardless of differential potentials. Electron emissions are also consistently detected around 180 deg azimuth with 0 deg elevation and −90 deg elevation, when the servicer is parallel to faces of the target that are also shielded from the components. This then leads to a relatively simple strategy to detect electron emissions from a spacecraft that may have differential potentials: the servicer should increase the distance between the possibly differentially charged components and itself. This may be feasible for scenarios in which the servicer is free to move to all relative locations about a target, such as electrostatic actuation operations. In other scenarios, such as docking, in which the servicer should remain near the docking port, the servicer can approach the target in a region with a larger number of detectable instances.

The appropriate servicer locations about the target vary with target geometry and must be evaluated for specific target geometry. It is also possible for unexpected differential potentials to form on the target, which can deflect electrons away from a region previously considered reliable for detecting electron emissions. To increase the reliability of sensing despite differential potentials, the servicer can sweep through relative positions until electron emissions are detected, or *x*-ray emissions can be used to determine the surface potential with higher uncertainty until electron emissions are detected.

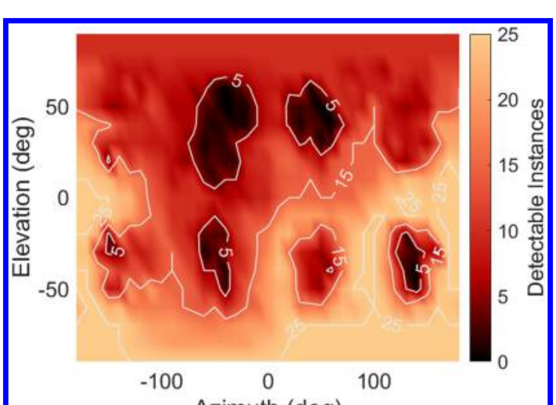

Fig. 8 Number of differential potential instances on the target in which the servicer detects electron emissions for varying azimuth and elevation.

IV. Electron Emission Equipment Parameters

A. Simulation Setup

Positioning the servicer about the target so that electron emissions can be detected is the first step to accurately determining the target's potential; however, the electron beam or VUV laser is not expected to fully envelop the target. As a result, even if the servicer is in the correct position, it is possible for the beam or laser to miss the region where emitted electrons reach the servicer, referred to as a *source region*. Previous experiments have not investigated how the electron beam or VUV parameters can be manipulated to find a source region. Therefore, the impact of equipment parameters, shown in Table 2, on detected electron emission current from a uniformly charged target is investigated to determine how the equipment can be manipulated to impact a source region. Once the best-case equipment parameters are defined, the servicer is moved in the same manner as described in Sec. III.A to quantify the change in observability with different equipment parameters. Last, differential potentials are defined on the target to investigate how the source region and emission equipment performance may change.

In this section, the servicer is held at an azimuth and elevation of 0 deg. If there is no deflection, the electron beam and VUV laser impact the center of the target's body, as shown in Fig. 9. It should be noted that the VUV laser itself likely cannot alter its deflection angle or half angle, and it is assumed that an external setup, such as a movable platform or opaque cover, is capable of changing these parameters. In Sec. III.C, it is shown that, in this location, electron emissions can reach the servicer for nine of the 25 surface potential combinations: when the components are equipotential with the main body or more positively charged.

The beam current and VUV laser energy are held constant in this section, and the effect of these parameters on the sensing and charging process is discussed in Sec. V. In addition, the beam current is well below the SCL currents previously presented in Fig. 3.

B. Uniform Target Potential

1. *Singular Position*

Figures 10 and 11 show the detected SE current as a function of the electron beam parameters and detected PE current as a function of the VUV laser parameters, respectively. For both, the maximum

Table 2 Equipment parameters

Parameter	Electron beam	VUV laser
Energy, E_B	1–30 keV	7.7 eV
Current, I_B	1 μA	N/A
Flux, f_{ph}	N/A	9.7E14 photons/s
Deflection angle, γ	−2 to 2 deg	−2 to 2 deg
Half angle, ϕ	0.2 to 2 deg	0.2 to 2 deg

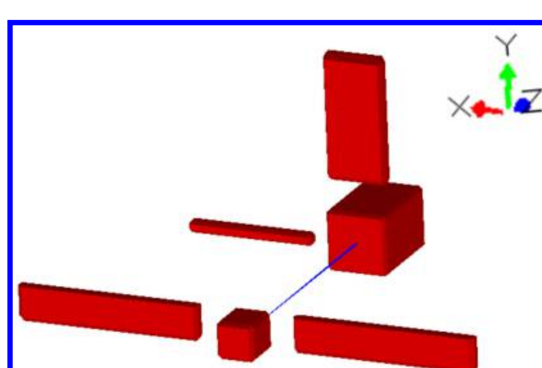

Fig. 9 Electron beam trajectory with no deflection.

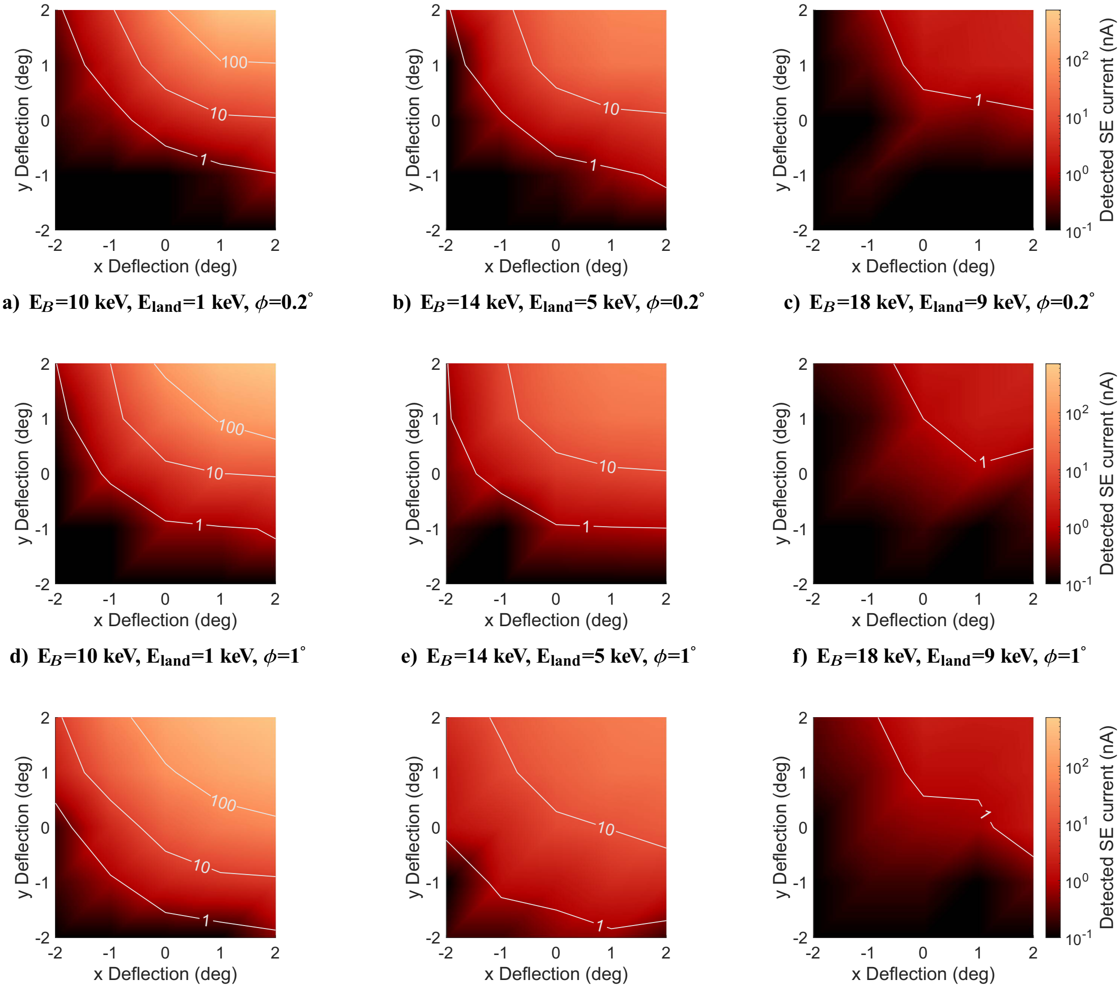

a) E_B=10 keV, E_{land}=1 keV, ϕ=0.2° b) E_B=14 keV, E_{land}=5 keV, ϕ=0.2° c) E_B=18 keV, E_{land}=9 keV, ϕ=0.2°

d) E_B=10 keV, E_{land}=1 keV, ϕ=1° e) E_B=14 keV, E_{land}=5 keV, ϕ=1° f) E_B=18 keV, E_{land}=9 keV, ϕ=1°

g) E_B=10 keV, E_{land}=1 keV, ϕ=2° h) E_B=14 keV, E_{land}=5 keV, ϕ=2° i) E_B=18 keV, E_{land}=9 keV, ϕ=2°

Fig. 10 Detected secondary electron current in nA for uniform spacecraft potentials.

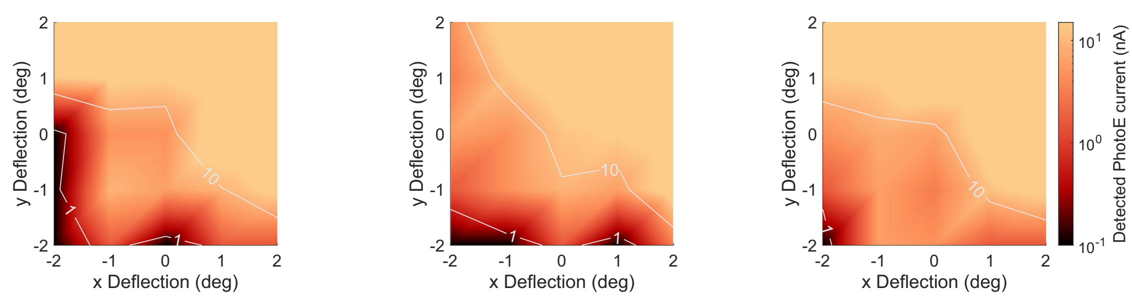

a) ϕ=0.2° b) ϕ=1° c) ϕ=2°

Fig. 11 Detected photoelectron current in nA for uniform spacecraft potentials.

current is detected when the deflection angle is $+2$ deg in the x and y directions. The x and y-axes are defined the same as previously shown in Fig. 9, so this deflection directs the beam toward both the boom and solar panel. The SEs and PEs generated on this corner of the target body are repelled by the boom and solar panel into the face of the servicer, making this the *source region* for this uniformly charged servicer–target orientation. As the deflection angles stray from the source region, the detected emission current decreases regardless of other parameters. Therefore, an appropriate deflection angle must be achieved, or emissions will not be detected.

Larger half angles increase the number of beam deflections at which electron emission current is detected. Increasing the half angle of the equipment increases the probability that at least part of the beam impacts the source region, increasing the observability. In fact, when the half angle of the VUV laser's beam is 2 deg, current is detected at every deflection angle except -2 deg in the x and y directions. It should be considered that only part of the beam impacts the source region for a larger half-angle, decreasing the detected current. In the range of half angles explored, the order of magnitude of the maximum detected emission current remains the same, but the detected current is expected to decrease as the half angle increases. This effect can be accounted for by increasing the beam current, minimizing the landing energy to increase the SE current, or increasing the VUV laser energy to increase the PE current. Once the source region is determined with a wide beam, the half angle can also be decreased to increase the detected current.

Minimizing the landing energy increases the number of deflection angles at which SE current is detected. This is surprising because higher-energy beams are less deflected by the electric field about the charged spacecraft and would be expected to more reliably impact the source region. However, SE emissions favor low-energy-impacting electrons, with the energy at which the maximum yield occurs E_{max} typically around a few hundred electron volts. Figure 12 shows the Sanders and Inouye SE yield model as a function of landing energy for materials commonly used on spacecraft [1,72]. As shown, once the landing energy exceeds E_{max}, the yield decreases, and at approximately 5 keV the yield is minimal for most of the example materials. Raising the beam energy ≈5 keV does not significantly change the trajectory in the electric field of these high-potential spacecraft, so the beam energy cannot be raised to decrease deflection within the energy range that significant SEs are emitted. Therefore, the focus should be to minimize the beam energy to increase SE yield. This could be achieved by first using x-ray emissions to obtain a rough estimate of the target's surface potential and then determining an appropriate beam energy for SE emission. Otherwise, the beam energies must be swept through until sufficient SEs are emitted. Because the VUV laser is not deflected by the ambient electric field, changing the flux or photon energy does not change where the VUV laser impacts, and these parameters are analogous to the electron beam current. This is discussed further in Sec. V.

2. *Variable Positions*

The beam and VUV laser are maintained at a constant half angle of 2 deg and deflected until at least 10 nA of current is detected or all deflection angles are tested at each servicer and target location. The electron beam maintains an energy of 10 keV and a current of 1 μA. There are 25 possible deflection angles tested at 703 servicer positions, for another 17,575 SIMION simulations for both the electron beam and VUV laser.

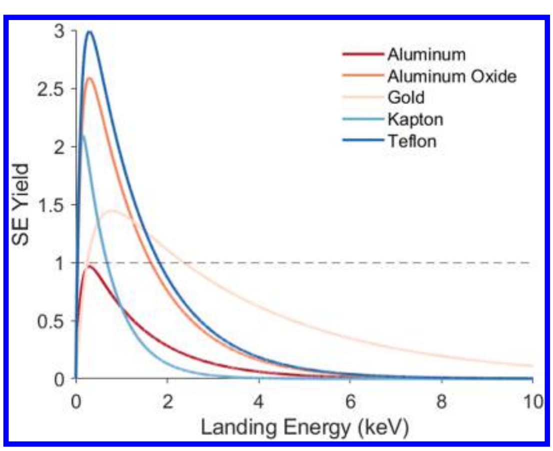

Fig. 12 Secondary electron yields for common spacecraft surface materials.

When using the electron beam, sufficient current is detected at 128 positions when the beam is not deflected and 242 positions when the beam is deflected. When using the VUV laser, sufficient current is detected at 133 positions without deflection and 241 positions with deflection. This represents a 90% and 81% increase in observability with the electron beam and VUV laser, respectively. In other words, the number of positions from which the servicer can determine the target's potential nearly *doubles* when the emission equipment is deflected.

The observability about the uniformly charged target is nearly the same with both the electron gun and VUV laser, regardless of the deflection of the equipment. Therefore, both options are viable for detecting the potential of a uniformly charged target.

C. Differential Target Potentials

Now, the electron beam and VUV laser maintain a half angle of 2 deg, the deflection angle is varied, and the energy of the electron beam is swept through while the servicer and target remain at 0 deg azimuth and elevation and the target is prescribed the same differential potentials set in Sec. III.C. As a reminder, emissions can be detected for nine of the 25 differential potential combinations at this location. SE emissions are detected for four of the possible nine surface potential combinations, regardless of beam energy, again indicating that increasing the beam energy does not increase the observability of electron emissions about a target. The four surface potential combinations that allow electron emission detection only include a solar panel or boom that is equipotential or 10 kV more positive than the main body. Outside of this range, the electron beam is deflected such that it does not impact the source region. Conversely, PE emissions are detected for all nine of the possible potential combinations, meaning full observability has been achieved. Because the VUV laser is not deflected by the ambient electric field, if there is a source region, the laser is capable of hitting it. The VUV laser is therefore more reliable than the electron beam when detecting the potential of a differentially charged target.

The detected currents from a differentially charged target for a 10 keV electron beam and the VUV laser are shown in Figs. 13 and 14, respectively. When the components are biased positively with respect to the main body, the source region moves *away* from the components to counteract the attractive force. Conversely, if the component is equal to or more negative than the main body, the source region moves *toward* it to counteract the repulsive force. This means that the electron beam and VUV laser cannot be repeatedly directed toward the same position on the target to emit detectable electrons if differential potentials occur. Conversely, if the source region is different than expected, it can be concluded that a nearby component is biased more positively if the source region moves farther from it or more negatively if the source region moves closer to it. This simplifies detection of differentially charged components, as the electron gun and VUV laser can be deflected to search for the component based on the change in the source region. In addition, insight into the potential magnitude of a nearby component can be achieved without directly detecting it. Since a VUV laser is not deflected by the ambient electric field and may create a spotlight on

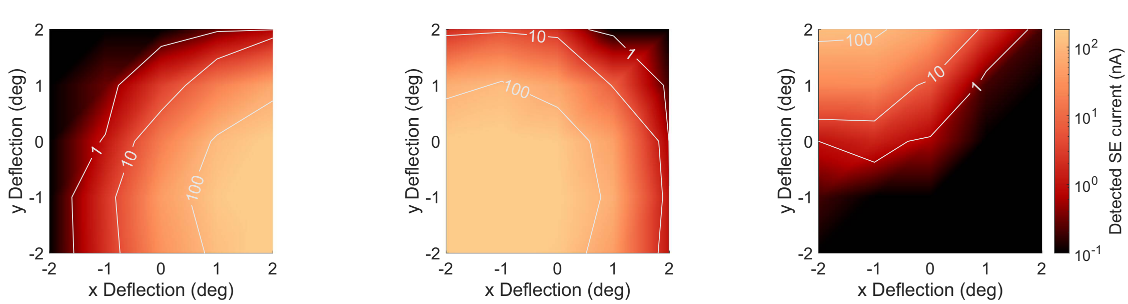

a) -13 keV boom, -3 keV SP b) -3 keV boom, -3 keV SP c) -3 keV boom, -13 keV SP

Fig. 13 Detected secondary electron current in nA for differential spacecraft potentials.

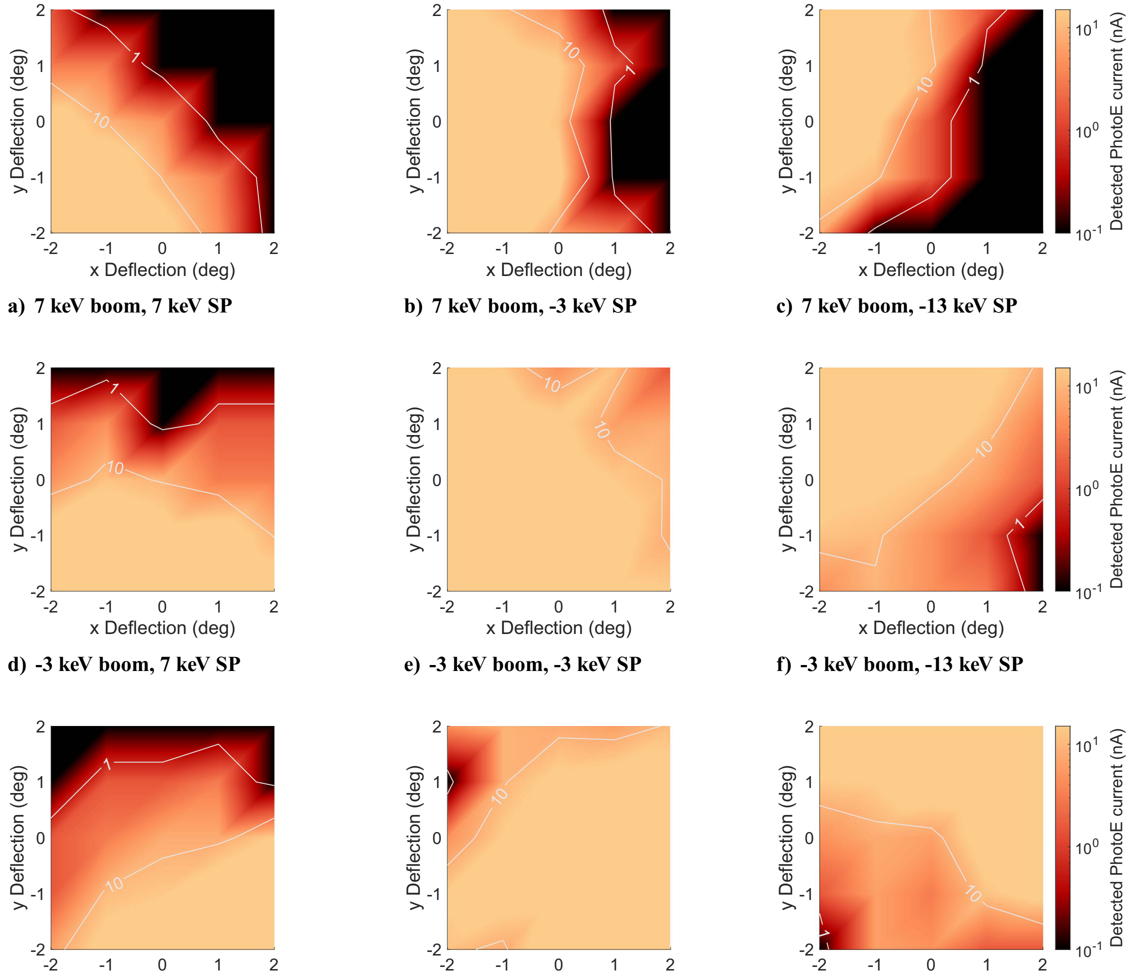

a) 7 keV boom, 7 keV SP
b) 7 keV boom, -3 keV SP
c) 7 keV boom, -13 keV SP
d) -3 keV boom, 7 keV SP
e) -3 keV boom, -3 keV SP
f) -3 keV boom, -13 keV SP
g) -13 keV boom, 7 keV SP
h) -13 keV boom, -3 keV SP
i) -13 keV boom, -13 keV SP

Fig. 14 Detected photoelectron current in nA for differential spacecraft potentials.

the target, it is likely simpler to determine which component is differentially charged using the VUV laser.

V. Charging Behavior

In the previous section, it is assumed that the electron beam and VUV laser are not changing the surface potentials of the target or servicer. This could be achieved by maintaining a sufficiently low electron beam current so that the spacecraft potentials remain unchanged [62] or by pulsing the electron beam [73]. These conditions may not be guaranteed, or the servicer could be purposely charging the target to perform electrostatic actuation. Previously, Romero-Calvo et al. [44] conducted a study to determine the output power and VUV laser energy required to charge various spacecraft in different environments. To summarize, the PE yield remains unchanged above a photon energy of ≈10 eV, so the output power must be increased to increase the PE yield above this energy. A higher-power and higher-energy VUV laser can be used to discharge a target, and a lower-power and lower-energy VUV laser is useful for sensing without charging the target. However, the VUV laser does not charge the servicer, so it cannot be guaranteed that the servicer will remain more positive than the target, which is necessary to detect electron emissions.

Because the impact of VUV laser energy and output power on target charging and sensing has been investigated, in this section, the beam energy and current at which the spacecraft begin to charge and the landing energy of the beam in the presence of varying spacecraft charges are evaluated. This is done for spacecraft in shadow because higher-magnitude spacecraft potentials are expected when the spacecraft are eclipsed, both with and without an electron beam in use [4,62,70]. The charging equations implemented for this configuration can be found in the Appendix.

The spacecraft charging and electron beam landing energy are analyzed in the average cislunar plasma sheet and magnetotail lobes plasma environments. The electron density, electron temperature, ion density, and ion temperature are 2.2E5 m^{-3}, 150 eV, 2E5 m^{-3}, and 780 eV, respectively, in the plasma sheet, and 2E5 m^{-3}, 48 eV, 2E5 m^{-3}, and 290 eV, respectively, in the magnetotail lobes, based on values in the Design Specification for Natural Environments (DSNE) [51].

Figure 15 shows the resulting spacecraft potentials and beam landing energy. The servicer charges the same regardless of beam energy because the surface potential does not exceed the energy of the beam, so all emitted electrons simply leave the servicer in all cases. The target charges more than 100 V once the beam current exceeds ≈1 μA regardless of beam energy. This is consistent with the maximum allowable current in GEO space found by Hammerl and Schaub in [62]. Therefore, below ≈1 μA, the beam energy must be swept through to find the appropriate energy to emit SEs, and it is likely that the spacecraft potentials will not be altered.

When the beam current exceeds ≈50–200 μA, depending on the beam energy and environment, the spacecraft continue to charge, but the landing energy flattens out between 1 and 5 keV. This simplifies the sensing process for electrostatic actuation operations because the landing energy remains in a range in which electron emissions are expected, eliminating the need to sweep through beam

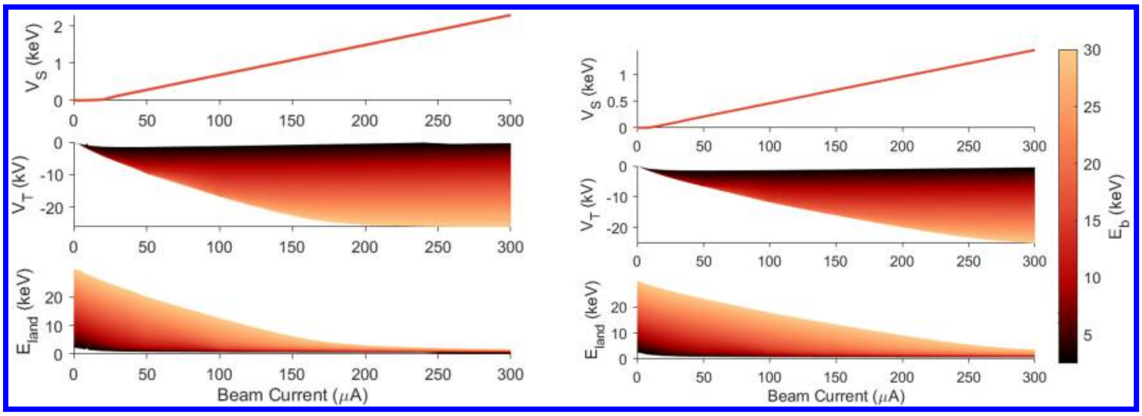

a) Plasmasheet **b) Magnetotail Lobes**

Fig. 15 Servicer and target potentials and beam landing energy in the plasma sheet and magnetotail lobes environments.

energies to emit SEs and simplifying the sensing process. If the SCL current is exceeded, it may be necessary to reduce the current and sweep through beam potentials. This also provides assurance that touchless potential sensing with SE emissions can likely be conducted during electrostatic actuation operations.

VI. Conclusions

This work presents new strategies to increase the observability of electron emissions for touchless spacecraft potential sensing, particularly in the presence of differential charging. The results demonstrate that electron emission trajectories are steady in the presence of a uniformly charged servicer and target. This allows the regions in which electron emissions penetrate around a target to be predetermined and integrated into spacecraft guidance controls, such as those developed in [11]. More significantly, it is shown that, with differentially charged targets, positively and negatively biased components shift the electron emission trajectories in predictable ways, which can be used to adjust the servicer position and equipment deflection. This also provides insight into the relative potential magnitude of components near the region being sensed.

Through extensive particle tracing simulations in SIMION, it is shown that observability can be nearly doubled by widening the electron beam or VUV laser and varying its deflection angle. Notably, the electron beam and VUV laser achieve comparable improvements in observability about a uniformly charged target, despite their different physical characteristics. However, around a differentially charged target, the electron beam cannot reliably be utilized to detect the target's potential due to beam deflection, while the VUV laser continues to reliably impact source regions.

It is also shown that the electron beam landing energy stabilizes between 1 and 5 keV during electrostatic actuation, efficiently generating electron emissions for sensing. This avoids the need to sweep through electron beam potentials to generate secondaries during electrostatic tractor operations.

The proposed strategies improve the reliability of touchless potential sensing using electron emissions in realistic proximity operation conditions. These findings provide practical guidance for safe spacecraft servicing, docking, and electrostatic actuation in high-potential environments such as GEO and cislunar space.

Appendix: Active Charging Equations

The potential of an eclipsed servicer equipped with an electron gun is determined using the current balance equation:

$$I_e(V)(1-\alpha) - I_i(V)(1-\delta_i) - I_B(V) = 0 \tag{A1}$$

where I_e is the incident electron current, I_i is the incident ion current, α is the sum of the SE yield δ and backscattered electron yield η, and δ_i is the SE due to incident ions yield. The orbit motion limited (OML) equations for spherical current collection are utilized, and the incident electron current is [1]

$$I_e = \frac{1}{4} q_e n_e v_e A \exp\left(\frac{q_e V}{k_B T_e}\right) \quad \text{for } V < 0 \tag{A2a}$$

$$I_e = \frac{1}{4} q_e n_e v_e A \left(1 + \frac{q_e V}{k_B T_e}\right) \quad \text{for } V > 0 \tag{A2b}$$

where A is the total surface area of the spacecraft. The incident ion current is similarly

$$I_i = \frac{1}{4} q_e n_i v_i A \left(1 - \frac{q_e V}{k_B T_i}\right) \quad \text{for } V < 0 \tag{A3a}$$

$$I_i = \frac{1}{4} q_e n_i v_i A \exp\left(\frac{-q_e V}{k_B T_i}\right) \quad \text{for } V > 0 \tag{A3b}$$

Hydrogen ions (H^+) are assumed.

The SE yield δ depends on the incidence energy of the primary particle and the angle of incidence. For this approximation, the incidence angle of the electrons is assumed to be zero, or perpendicular to the surface of the spacecraft, so δ can be roughly approximated by the Sanders and Inouye yield model [72]:

$$\delta(E,0) = c[e^{-E/a} - e^{-E/b}] \tag{A4}$$

where $a = 4.3E_{\max}$, $b = 0.367E_{\max}$, and $c = 1.37\delta_{\max}$ [72]. The values for aluminum are again used for $\delta_{\max}$ and $E_{\max}$.

The backscattered electron yield η for sufficient incidence energy depends on the atomic number of the surface material Z and the impact angle. For this approximation, the incidence angle is once again assumed to be zero, and the yield is approximated by the model proposed by Everhart [74]:

$$\eta(Z,0) = \frac{a - 1 + 0.5^a}{a + 1} \tag{A5}$$

with $a(Z) = 0.045Z$ being an experimentally fitted parameter. The minimum electron energy (in eV) that makes this approach valid is shown to be

$$E_{\min} \geq 13.7Z^{4/3} \tan(\theta/2) \tag{A6}$$

with $180\ \text{deg} - \theta$ being the deflection angle of the electron in the material, and $\theta = 45\ \text{deg}$ based on the suggestion made by Everhart [74]. If the impact energy is smaller than $E_{\min}$, the backscattered electron current is assumed to be negligible. The atomic number of aluminum is 13 [68], resulting in a minimum energy for backscattered electron emissions of 173.46 eV.

SE emissions escape from the surface with energies on the order of a few volts, while backscattered electrons are emitted with their approximate impact energy. Therefore, if the spacecraft is more than a few volts positive, the SE emissions will be attracted back toward the servicer. In order to find α in a Maxwellian plasma, the yield is integrated over the distribution function. As a result, the electron emission yield is modeled as

$$\alpha = \int_0^\infty (\eta(E) + \delta(E)) f_E(E)\,\mathrm{d}E \quad \text{for } V < 0 \tag{A7a}$$

$$\alpha = \int_0^\infty \left(\eta(E) + \delta(E)\exp\left(\frac{-V}{k_B T_{\mathrm{se}}}\right)\right) f_E(E)\,\mathrm{d}E \quad \text{for } V > 0 \tag{A7b}$$

where T_{se} is the dominant emission energy of SEs, assumed to be 1.333 eV, and $f_E(E)$ is the Maxwellian energy distribution function:

$$f_E(E) = \frac{2E^{1/2}}{\pi^{1/2}(k_B T_e)^{3/2}} \exp\left(\frac{-E}{k_B T_e}\right) \tag{A8}$$

The SE yield due to incoming ions is based on the Nascap-2k implementation [75]:

$$\delta_i(E) = \frac{\beta E^{1/2}}{1 + E/E_{\max,i}} \quad \text{for } V < 0 \tag{A9a}$$

$$\delta_i(E) = \frac{\beta E^{1/2}}{1 + E/E_{\max,i}} \exp\left(\frac{-V}{k_B T_{\mathrm{se}}}\right) \quad \text{for } V > 0 \tag{A9b}$$

where β is a scaling parameter and $E_{\max,i}$ is the ion energy at which the maximum yield occurs. Values of 0.244 and 230 keV for β and $E_{\max,i}$ are based on the values for aluminum implemented in Nascap-2k.

The current balance equation of a target being impacted by an electron beam, assuming that the entirety of the beam impacts the target, is

$$I_e(V)(1-\alpha) - I_i(V)(1-\delta_i) + I_B(V)(1-\alpha_B) = 0 \tag{A10}$$

where α_B is the sum of the SE and backscattered electron emissions due to the beam. The landing energy of the electron beam is

$$E_{\mathrm{land}} = E_B + q_e V_t - q_e V_s \quad \text{for } q_e V_s - q_e V_t < E_B \tag{A11}$$

$$E_{\mathrm{land}} = 0 \quad \text{for } q_e V_s - q_e V_t \geq E_B \tag{A12}$$

If the difference between the potential of the servicer and the target is greater than the energy of the electron beam ($q_e V_s - q_e V_t \geq E_B$), the beam will be deflected by both objects and will not impact the target. The landing energy of the electron beam then serves as the impact energy when calculating α_B using Eq. (A7a).

Acknowledgments

This work is supported by a NASA Space Technology Graduate Research Opportunity Grant Number 80NSSC22K1175 and the U.S. Air Force Office of Scientific Research under grant FA9550-23-S-0570. The authors would like to thank Álvaro Romero-Calvo for his fruitful discussion on the complexities of touchless potential sensing using electron emissions and David Manura (Adaptas Solutions LLC) for his assistance with the development of the SIMION simulation framework. AI was used to assist with the editing of this paper.

References

[1] Lai, S. T., *Fundamentals of Spacecraft Charging: Spacecraft Interactions with Space Plasmas*, Preton Univ. Press, Princeton, NJ, 2012.

[2] Garrett, H. B., and Whittlesey, A. C., "Spacecraft Design Guidelines," *Guide to Mitigating Spacecraft Charging Effects*, Vol. 3, Wiley, Hoboken, NJ, 2012, pp. 26–61, Chap. 3. https://doi.org/10.1002/9781118241400.ch3

[3] Roe, R., *Mitigating In-Space Charging Effects-A Guideline*, National Aeronautics and Space Administration, Washington, D.C., 2022, pp. 10–13.

[4] Willis, E., Diekmann, A., and Guy, M., "Plasma Charging of Crewed Spacecraft in Lunar Orbit," *Space Environment Engineering and Science Applications Workshop*, Johns Hopkins University Applied Physics Laboratory, 2022.

[5] Olsen, R. C., McIlwain, C. E., and Whipple, E. C., Jr., "Observations of Differential Charging Effects on ATS. 6," *Journal of Geophysical Research: Space Physics*, Vol. 86, No. A8, 1981, pp. 6809–6819. https://doi.org/10.1029/JA086iA08p06809

[6] Roeder, J. L., and Fennell, J. F., "Differential Charging of Satellite Surface Materials," *IEEE Transactions on Plasma Science*, Vol. 37, No. 1, 2009, pp. 281–289. https://doi.org/10.1109/TPS.2008.2004765

[7] Lai, S., "A Critical Overview on Spacecraft Charging Mitigation Methods," *IEEE Transactions on Plasma Science*, Vol. 31, No. 6, 2003, pp. 1118–1124. https://doi.org/10.1109/TPS.2003.820969

[8] Garrett, H., and Whittlesey, A., "Spacecraft Charging, an Update," *IEEE Transactions on Plasma Science*, Vol. 28, No. 6, 2000, pp. 2017–2028. https://doi.org/10.1109/27.902229

[9] Cho, M., Kawakita, S., Nakamura, M., Takahashi, M., Sato, T., and Nozaki, Y., "Number of Arcs Estimated on Solar Array of a Geostationary Satellite," *Journal of Spacecraft and Rockets*, Vol. 42, No. 4, 2005, pp. 740–748. https://doi.org/10.2514/1.6694

[10] Wilson, K. T. H., and Schaub, H., "Impact Of Electrostatic Perturbations on Proximity Operations In High Earth Orbits," *AIAA Journal of Spacecraft and Rockets*, Vol. 58, No. 5, 2021, pp. 1293–1302. https://doi.org/10.2514/1.A35039

[11] Wilson, K. T. H., Romero Calvo, Á., and Schaub, H., "Constrained Guidance for Spacecraft Proximity Operations Under Electrostatic Perturbations," *Journal of Spacecraft and Rockets*, Vol. 59, No. 4, 2022, pp. 1304–1316. https://doi.org/10.2514/1.A35162

[12] Hogan, E. A., and Schaub, H., "Impacts of Tug and Debris Sizes on Electrostatic Tractor Charging Performance," *Advances in Space Research*, Vol. 55, No. 2, 2015, pp. 630–638. https://doi.org/10.1016/j.asr.2014.10.023

[13] Hogan, E. A., and Schaub, H., "Impacts of Hot Space Plasma and Ion Beam Emission on Electrostatic Tractor Performance," *IEEE Transactions on Plasma Science*, Vol. 43, No. 9, 2014, pp. 3115–3129. https://doi.org/10.1109/TPS.2015.2451001

[14] Bengtson, M., Wilson, K. T. H., Hughes, J., and Schaub, H., "Survey of the Electrostatic Tractor Research for Reorbiting Passive GEO Space Objects," *Astrodynamics*, Vol. 2, No. 4, 2018, pp. 291–305. https://doi.org/10.1007/s42064-018-0030-0

[15] Hughes, J., and Schaub, H., "Electrostatic Tractor Analysis Using a Measured Flux Model," *AIAA Journal of Spacecraft and Rockets*, Vol. 57, No. 2, 2020, pp. 207–216. https://doi.org/10.2514/1.A34359

[16] Hammerl, J., and Schaub, H., "Effects of Electric Potential Uncertainty on Electrostatic Tractor Relative Motion Control Equilibria," *Journal of Spacecraft and Rockets*, Vol. 59, No. 2, 2022, pp. 552–562. https://doi.org/10.2514/1.A35165

[17] Bennett, T., Stevenson, D., Hogan, E., McManus, L., and Schaub, H., "Prospects and Challenges of Touchless Debris Despinning Using Electrostatics," *Advances in Space Research*, Vol. 56, No. 3, 2015, pp. 557–568. https://doi.org/10.1016/j.asr.2015.03.037

[18] Bennett, T., and Schaub, H., "Contactless Electrostatic Detumbling of Axi-Symmetric GEO Objects with Nominal Pushing or Pulling," *Advances in Space Research*, Vol. 62, No. 11, 2018, pp. 2977–2987. https://doi.org/10.1016/j.asr.2018.07.021

[19] Aslanov, V., and Schaub, H., "Detumbling Attitude Control Analysis Considering an Electrostatic Pusher Configuration," *AIAA Journal of Guidance, Control, and Dynamics*, Vol. 42, No. 4, 2019, pp. 900–909. https://doi.org/10.2514/1.G003966

[20] Casale, F., Schaub, H., and Biggs, J. D., "Lyapunov Optimal Touchless Electrostatic Detumbling of Space Debris in GEO Using a Surface Multisphere Model," *Journal of Spacecraft and Rockets*, Vol. 58, No. 3, 2021, pp. 764–778.
https://doi.org/10.2514/1.A34787

[21] Mandell, M., Davis, V., Cooke, D., Wheelock, A., and Roth, C., "Nascap-2k Spacecraft Charging Code Overview," *IEEE Transactions on Plasma Science*, Vol. 34, No. 5, 2006, pp. 2084–2093.
https://doi.org/10.1109/TPS.2006.881934

[22] Thiébault, B., Jeanty-Ruard, B., Souquet, P., Forest, J., Matéo-Vélez, J.-C., Sarrailh, P., Rodgers, D., Hilgers, A., Cipriani, F., Payan, D., et al., "SPIS. 5.1: An Innovative Approach for Spacecraft Plasma Modeling," *IEEE Transactions on Plasma Science*, Vol. 43, No. 9, 2015, pp. 2782–2788.
https://doi.org/10.1109/TPS.2015.2425300

[23] Engelhart, D., Cooper, R., Cowardin, H., Maxwell, J., Plis, E., Ferguson, D., Barton, D., Schiefer, S., and Hoffmann, R., "Space Weathering Experiments on Spacecraft Materials," *Journal of the Astronautical Sciences*, Vol. 66, No. 2, 2019, pp. 210–223.
https://doi.org/10.1007/s40295-019-00175-2

[24] de Groh, K. K., Banks, B. A., Miller, S. K., and Dever, J. A., "Chapter 28—Degradation of Spacecraft Materials," *Handbook of Environmental Degradation of Materials*, edited by M. Kutz, 3rd ed., William Andrew Publ., Cambridge, MA, 2018, pp. 601–645.
https://doi.org/10.1016/B978-0-323-52472-8.00029-0

[25] Denton, M. H., Thomsen, M. F., Korth, H., Lynch, S., Zhang, J. C., and Liemohn, M. W., "Bulk Plasma Properties at Geosynchronous Orbit," *Journal of Geophysical Research: Space Physics*, Vol. 110, No. A7, July 2005.
https://doi.org/10.1029/2004JA010861

[26] Ferguson, D. C., Murray-Krezan, J., Barton, D. A., Dennison, J. R., and Gregory, S. A., "Feasibility of Detecting Spacecraft Charging and Arcing by Remote Sensing," *Journal of Spacecraft and Rockets*, Vol. 51, No. 6, 2014, pp. 1907–1913.
https://doi.org/10.2514/1.A32958

[27] Halekas, J. S., Lin, R. P., and Mitchell, D. L., "Large Negative Lunar Surface Potentials in Sunlight and Shadow," *Geophysical Research Letters*, Vol. 32, No. 9, 2005.
https://doi.org/10.1029/2005GL022627

[28] Halekas, J., Delory, G., Lin, R., Stubbs, T., and Farrell, W., "Lunar Prospector Observations of the Electrostatic Potential of the Lunar Surface and Its Response to Incident Currents," *Journal of Geophysical Research: Space Physics*, Vol. 113, No. A9, 2008.
https://doi.org/10.1029/2008JA013194

[29] Halekas, J. S., Delory, G. T., Lin, R. P., Stubbs, T. J., and Farrell, W. M., "Lunar Surface Charging During Solar Energetic Particle Events: Measurement and Prediction," *Journal of Geophysical Research: Space Physics*, Vol. 114, No. A5, 2009.
https://doi.org/10.1029/2009JA014113

[30] Poppe, A., Halekas, J. S., and Horányi, M., "Negative Potentials Above the Day-Side Lunar Surface in the Terrestrial Plasma Sheet: Evidence of Non-Monotonic Potentials," *Geophysical Research Letters*, Vol. 38, No. 2, 2011.
https://doi.org/10.1029/2010GL046119

[31] Halekas, J., Saito, Y., Delory, G., and Farrell, W., "New Views of the Lunar Plasma Environment," *Planetary and Space Science*, Vol. 59, No. 14, 2011, pp. 1681–1694.
https://doi.org/10.1016/j.pss.2010.08.011

[32] Sagüés, A. A., and Walsh, M. T., "Kelvin Probe Electrode for Contactless Potential Measurement on Concrete—Properties and Corrosion Profiling Application," *Corrosion Science*, Vol. 56, March 2012, pp. 26–35.
https://doi.org/10.1016/j.corsci.2011.11.007

[33] LaPointe, M., Esser, B., Aponte, I., Cardenas, Z., Dickens, J., Mankowski, J., Stephens, J., Friesen, D., Nelson, C., Koone, N., et al., "Surface Charge Distribution Mapping Using an Electrostatic Probe," *2021 IEEE Pulsed Power Conference (PPC)*, Inst. of Electrical and Electronics Engineers, New York, 2021, pp. 1–5.
https://doi.org/10.1109/PPC40517.2021.9733129

[34] Amiour, N., Zeghloul, T., Bendilmi, M. S., and Dascalescu, L., "Comparison and Calibration of Four Instruments for the Measurement of Electric Potential at the Surface of Non-Planar Bodies," *Journal of Electrostatics*, Vol. 134, March 2025, Paper 104041.
https://doi.org/10.1016/j.elstat.2025.104041

[35] Heath, J. T., Jiang, C.-S., and Al-Jassim, M. M., "Measurement of Semiconductor Surface Potential Using the Scanning Electron Microscope," *Journal of Applied Physics*, Vol. 111, No. 4, 2012, Paper 046103.
https://doi.org/10.1063/1.3684556

[36] Bengtson, M., Hughes, J., and Schaub, H., "Prospects and Challenges for Touchless Sensing of Spacecraft Electrostatic Potential Using Electrons," *IEEE Transactions on Plasma Science*, Vol. 47, No. 8, 2019, pp. 3673–3681.
https://doi.org/10.1109/TPS.2019.2912057

[37] Bengtson, M. T., and Schaub, H., "Electron-Based Touchless Potential Sensing of Shape Primitives and Differentially-Charged Spacecraft," *Journal of Spacecraft and Rockets*, Vol. 58, No. 6, 2021, pp. 1847–1857.
https://doi.org/10.2514/1.A35086

[38] Bengtson, M. T., Wilson, K. T., and Schaub, H., "Experimental Results of Electron Method for Remote Spacecraft Charge Sensing," *Space Weather—The International Journal of Research and Applications*, Vol. 18, No. 3, 2020, pp. 1–12.
https://doi.org/10.1029/2019SW002341

[39] Romero Calvo, Á., Hammerl, J., and Schaub, H., "Touchless Potential Sensing of Complex Differentially-Charged Shapes Using Secondary Electrons," *AIAA Journal of Spacecraft and Rockets*, Vol. 59, No. 5, 2022, pp. 1623–1633.
https://doi.org/10.2514/1.A35355

[40] Wilson, K. T. H., and Schaub, H., "X-Ray Spectroscopy for Electrostatic Potential and Material Determination of Space Objects," *IEEE Transactions on Plasma Science*, Vol. 47, No. 8, 2019, pp. 3858–3866.
https://doi.org/10.1109/TPS.2019.2910576

[41] Wilson, K. T., Bengtson, M. T., and Schaub, H., "X-Ray Spectroscopic Determination of Electrostatic Potential and Material Composition for Spacecraft: Experimental Results," *Space Weather—The International Journal of Research and Applications*, Vol. 18, No. 4, 2020, Paper e2019SW002342.
https://doi.org/10.1029/2019SW002342

[42] Wilson, K. T. H., Hammerl, J., and Schaub, H., "Using Plasma-Induced X-Ray Emission to Estimate Electrostatic Potentials on Nearby Space Objects," *Journal of Spacecraft and Rockets*, Vol. 59, No. 4, 2022, pp. 1402–1405.
https://doi.org/10.2514/1.A35161

[43] Hammerl, J., López, A., Romero Calvo, Á., and Schaub, H., "Touchless Potential Sensing of Differentially Charged Spacecraft Using X-Rays," *Journal of Spacecraft and Rockets*, Vol. 60, No. 2, 2023, pp. 648–658.
https://doi.org/10.2514/1.A35492

[44] Romero Calvo, Á., Champion, K., and Schaub, H., "Enabling Ultraviolet Lasers for Touchless Spacecraft Potential Sensing," *IEEE Transactions on Plasma Science*, Vol. 51, No. 9, 2023, pp. 2468–2481.
https://doi.org/10.1109/TPS.2023.3264914

[45] Lai, S. T., and Miller, C., "Retarding Potential Analyzer: Principles, Designs, and Space Applications," *AIP Advances*, Vol. 10, No. 9, 2020, Paper 095324.
https://doi.org/10.1063/5.0014266

[46] Goembel, L., and Doering, J. P., "Instrument for Measuring Spacecraft Potential," *Journal of Spacecraft and Rockets*, Vol. 35, No. 1, 1998, pp. 66–72.
https://doi.org/10.2514/3.26999

[47] Schmidt, R., Arends, H., Pedersen, A., Rüdenauer, F., Fehringer, M., Narheim, B. T., Svenes, R., Kvernsveen, K., Tsuruda, K., Mukai, T., et al., "Results from Active Spacecraft Potential Control on the Geotail Spacecraft," *Journal of Geophysical Research: Space Physics*, Vol. 100, No. A9, 1995, pp. 17,253–17,259.
https://doi.org/10.1029/95JA01552

[48] Wilson, K. T. H., Bengtson, M., and Schaub, H., "Remote Electrostatic Potential Sensing for Proximity Operations: Comparison and Fusion of Methods," *Journal of Spacecraft and Rockets*, Vol. 59, No. 5, 2022, pp. 1425–1436.
https://doi.org/10.2514/1.A35071

[49] Bengtson, M., and Schaub, H., "Electron-Based Touchless Potential Sensing of Shape Primitives and Differentially-Charged Spacecraft," *AIAA Journal of Spacecraft and Rockets*, Vol. 58, No. 6, 2021, pp. 1847–1857.
https://doi.org/10.2514/1.A35086

[50] Debye, V., and Hückel, E., "Zur Theorie der Electrolyte," *Phyikalishce Zeitschrift*, Vol. 9, May 1923, pp. 185–206, https://knowledge.electrochem.org/estir/hist/hist-12-Debye-1.pdf.

[51] Leahy, F. B., "SLS-SPEC-159, Cross-Program Design Specification for Natural Environments (DSNE)," TR, Revision 1, NASA, 2021.

[52] Stevenson, D., and Schaub, H., "Multi-Sphere Method for Modeling Electrostatic Forces and Torques," *Advances in Space Research*, Vol. 51, No. 1, 2013, pp. 10–20.
https://doi.org/10.1016/j.asr.2012.08.014

[53] Stevenson, D., and Schaub, H., "Optimization of Sphere Population for Electrostatic Multi Sphere Model," *IEEE Transactions on Plasma

Science, Vol. 41, No. 12, 2013, pp. 3526–3535. https://doi.org/10.1109/TPS.2013.2283716

[54] Hughes, J., and Schaub, H., "Heterogeneous Surface Multi-Sphere Models Using Method of Moments Foundations," *Journal of Spacecraft and Rockets*, Vol. 56, No. 4, 2019, pp. 1259–1266. https://doi.org/10.2514/1.A34434

[55] Schaub, H., and Jasper, L. E. Z., "Orbit Boosting Maneuvers for Two-Craft Coulomb Formations," *AIAA Journal of Guidance, Control, and Dynamics*, Vol. 36, No. 1, 2013, pp. 74–82. https://doi.org/10.2514/1.57479

[56] Jasper, L. E., and Schaub, H., "Effective Sphere Modeling for Electrostatic Forces on a Three-Dimensional Spacecraft Shape," *AAS/AIAA Spaceflight Mechanics Meeting*, AAS Paper 11-465, 2011.

[57] Feuerbacher, B., and Fitton, B., "Experimental Investigation of Photoemission from Satellite Surface Materials," *Journal of Applied Physics*, Vol. 43, No. 4, 1972, pp. 1563–1572. https://doi.org/10.1063/1.1661362

[58] Meng, C.-I., and Mihalov, J. D., "Average Plasma-Sheet Configuration Near 60 Earth Radii," *Journal of Geophysical Research*, Vol. 77, No. 10, 1972, pp. 1739–1755. https://doi.org/10.1029/JA077i010p01739

[59] Livadiotis, G., "Collision Frequency and Mean Free Path for Plasmas Described by Kappa Distributions," *AIP Advances*, Vol. 9, No. 10, 2019, Paper 105307. https://doi.org/10.1063/1.5125714

[60] Child, C. D., "Discharge from Hot CaO," *Physical Review (Series I)*, Vol. 32, No. 5, 1911, pp. 492–511. https://doi.org/10.1103/PhysRevSeriesI.32.492

[61] Langmuir, I., "The Effect of Space Charge and Initial Velocities on the Potential Distribution and Thermionic Current Between Parallel Plane Electrodes," *Physical Review*, Vol. 21, No. 4, 1923, pp. 419–435. https://doi.org/10.1103/PhysRev.21.419

[62] Hammerl, J., and Schaub, H., "Coupled Spacecraft Charging Due to Continuous Electron Beam Emission and Impact," *Journal of Spacecraft and Rockets*, Vol. 61, No. 5, 2024, pp. 1258–1271. https://doi.org/10.2514/1.A36010

[63] Sun, H., Chen, J., Kaganovich, I. D., Khrabrov, A., and Sydorenko, D., "Physical Regimes of Electrostatic Wave-Wave Nonlinear Interactions Generated by an Electron Beam Propagating in a Background Plasma," *Physical Review E*, Vol. 106, No. 3, 2022, Paper 035203. https://doi.org/10.1103/PhysRevE.106.035203

[64] Gomberoff, K., Gomberoff, L., and Astudillo, H. F., "Ion-Beam–Plasma Electromagnetic Instabilities," *Journal of Plasma Physics*, Vol. 64, No. 1, 2000, pp. 75–87. https://doi.org/10.1017/S0022377800008436

[65] Dieckmann, M. E., and Shukla, P. K., "Electron Surfing Acceleration by the Electron Two-Stream Instability in a Weak Magnetic Field," *Plasma Physics and Controlled Fusion*, Vol. 48, No. 10, 2006, pp. 1515–1530. https://doi.org/10.1088/0741-3335/48/10/005

[66] Chung, M. S., and Everhart, T. E., "Simple Calculation of Energy Distribution of Low-Energy Secondary Electrons Emitted from Metals Under Electron Bombardment," *Journal of Applied Physics*, Vol. 45, No. 2, 1974, pp. 707–709. https://doi.org/10.1063/1.1663306

[67] Lai, S., and Tautz, M., "Aspects of Spacecraft Charging in Sunlight," *IEEE Transactions on Plasma Science*, Vol. 34, No. 5, 2006, pp. 2053–2061. https://doi.org/10.1109/TPS.2006.883362

[68] Lide, D. R., *CRC Handbook of Chemistry and Physics*, 84th ed., CRC Press, Boca Raton, FL, 2003, p. 123, Chap. 12.

[69] Champion, K., and Schaub, H., "Electrostatic Potential Shielding in Representative Cislunar Regions," *IEEE Transactions on Plasma Science*, Vol. 51, No. 9, 2023, pp. 2482–2500. https://doi.org/10.1109/TPS.2023.3236246

[70] McCollum, M., Willis, E., and Diekmann, A., "Artemis IV Docking in Radiation Belt Charging Environment," Aug. 2023, https://spaceweathersolutions.com/proceedings/.

[71] Ferguson, D. C., "Chapter 15—Extreme Space Weather Spacecraft Surface Charging and Arcing Effects," *Extreme Events in Geospace*, edited by N. Buzulukova, Elsevier, New York, 2018, pp. 401–418. https://doi.org/10.1016/B978-0-12-812700-1.00015-7

[72] Sanders, N., and Inouye, G., "Secondary Emission Effects on Spacecraft Charging: Energy Distribution Considerations," *Spacecraft Charging Technology-1978*, Vol. 2071, June 1979, pp. 747–755, https://adsabs.harvard.edu/full/1979NASCP2071.747S.

[73] Hammerl, J., "Coupled Interactions Between Charged Spacecraft: Relative Motion, Charging and Sensing," Ph.D. Thesis, Aerospace Engineering Sciences Dept., Univ. of Colorado, Boulder, CO, 2025.

[74] Everhart, T. E., "Simple Theory Concerning the Reflection of Electrons from Solids," *Journal of Applied Physics*, Vol. 31, No. 8, 1960, pp. 1483–1490. https://doi.org/10.1063/1.1735868

[75] Davis, V., and Mandell, M., "Nascap-2k Version 4.4 Scientific Documentation," 2020.

M. L. Walker
Associate Editor